Desalination and Water Treatment
www.deswater.com

doi:10.5004/dwt.2019.23288

139 (2019) 174–190
January

Investigation of the equilibrium, thermodynamic and kinetic parameters of study of the Allura red dye efficient removal from aqueous solution by magnetic α-Fe_2O_3 nanoparticles and its nanocomposite with graphite powder (α-Fe_2O_3/G-p)

Tanveer ul Haq Zia[a,*], Abdul Hadi Mehmood[a], Behisht Ara[b], Kashif Gul[b]

[a]*Department of Chemistry, Sarhad University of Science and IT, LandiAkhun Ahmad, Hayatabad Link Ring road, Peshawar (Khyber Pakhtunkhwa), 25000, Pakistan, Tel. +92-334 9011757, email: tanveerics@gmail.com (T.U.H. Zia), abdulhadimehmood15@gmail.com (A.H. Mehmood)*

[b]*Institute of Chemical Sciences,University of Peshawar, Jamrud road, Peshawar (Khyber Pakhtunkhwa), 25000, Pakistan, email: bahishtara@gmail.com (B. Ara), kashifpkh@yahoo.com (K. Gul)*

Received 26 May 2018; Accepted 14 October 2018

ABSTRACT

The adsorption of Allura red by magnetic α-Fe_2O_3 nanoparticles and its nanocomposite with graphite powder(α-Fe_2O_3/G-p) was studied using equilibrium, kinetics and thermodynamics adsorption models. The morphological and structural impact of α-Fe_2O_3 nanoparticles onto G-p was evaluated by using scanning electron microscopy (SEM) and wide angle X-ray diffraction (WAXD). BET model used for specific surface area analysis revealed values of 186.88 m^2/g for α-Fe_2O_3 nanoparticles and 349.85 m^2/g for nanocomposite whereas BJH model was employed to evaluate the pore size and pore size distribution confirming the mesoporous texture of adsorbents. The dependence of adsorption of Allura red dye by α-Fe_2O_3 nanoparticles and α-Fe_2O_3/G-p nanocomposite, on contact time, adsorbent dosage and pH was also evaluated. Adsorption equilibrium data was evaluated at different temperatures by applying Freundlich, Langmuir and Dubinin-Radushkevich (D-R) isotherms linear equations, on which statistical analysis was performed, revealing the important adsorption parameters such as R_L value of Langmuir model which confirms the physical adsorption phenomenon whereas *1/n* factor of Freundlich model highlights the favorable interaction between adsorbate and adsorbent. Pseudo-first-order, pseudo-second-order and intra-particle diffusion models were used for kinetics data analysis. The correlation factor R^2 is greater than 0.99 for pseudo second order model values confirming the multi step nature of adsorption. The Van't Hoff plots were plotted for obtaining the thermodynamic parameters of entropy change (ΔS), Gibb's free energy (ΔG) and the enthalpy (ΔH). The negative values of ΔG confirm the feasible spontaneous nature of adsorption process respectively.

Keywords: Allura red; BJH; Graphite powder; Langmuir; Magnetic nanoparticles; Pore size distribution; Spontaneous

1. Introduction

One of the leading sources of artificial dye's discharge into environment is the food coloring industry which makes use of food colorants such as indigo carmine, tartrazine, quinoline yellow WS, sunset yellow FCF and Allura red AC among which Allura red AC is widely used synthetic azo dye [1]. These colored discharges from the food industry into the water sources are of considerable concern, as it is one of the prime causes of eutrophication, by breaking off the re-oxygenation capacity of water as a result of sunlight blockage and can be transformed into

---

*Corresponding author.

toxic byproducts during its chemical degradation in environment resulting in the disturbance of aquatic life [2]. The persistent nature of the azo dyes render them stable to aerobic degradation by microorganisms whereas their anaerobic degradation results in the reduction of the azo linkage to colorless carcinogenic aromatic amines which can result in bladder cancer [3].

The removal of dyes from the waste water includes physico-chemical and bio-treatment. The bio-treatment mainly includes the aerobic degradation of dye by indigenous soil microorganisms, which renders it ineffective as the artificial dyes are resistant to aerobic biodegradation since they are chemically stable and only prone to anaerobic degradation [4]. The process of photocatalysis for decolorization has also been developed which mostly employs semi-conductor inorganic material such as TiO_2 which has severe hindrance of catalyst reuse after water treatment which makes it an expensive process [5]. The dye removal by other methods, such as chemical precipitation, chemical oxidation are very successful but their effectiveness is strongly influenced by the toxicity of oxidant as the methyl red degradation depends upon the Fe^{2+} ions and hydrogen peroxide employed for oxidation [6]. Similarly the flocculants also has detrimental effects on water quality [7].

Among all the methods developed for dye removal, adsorption is the most efficient and cost effective method which makes the waste water treatment economical. Activated carbon prepared from biomass has been used previously by Sharma et al. for the removal of congo red which showed maximum adsorption capacity of 68.96 mg/g from aqueous solutions [8]. Albadarin et al. carried out the studies on equilibrium and kinetic of methylene blue (M.B) dye removal by activated lignin-chitosan extruded (ALiCE) pellets which have highly developed porous structure for effective adsorption showing maximum adsorption capacity of 36.25 mg/g [9]. Furthermore, studies have also been carried out by Naushad et al. on amberlite IRA-938 resin system for the removal of Bengal dye from aqueous solution showing maximum adsorption capacity of 142.86 mg/g at 23°C [10]. Similarly removal of bromothymol blue (BTB) by magnetic Fe_2O_3/chitosan-bamboo saw dust (FeCBSD) composite has also been carried out [11]. In addition magnetically modified multiwalled carbon nanotubes have also been employed for removal of bismarck brown R and Cd(II) from aqueous solution showing an adsorption capacity (q_m) of 76.92 and 38.17 mg/g for BBR and Cd(II), respectively [12].

The magnetic iron oxide hematite α-Fe_2O_3 nanoparticles have edge over other absorbents of being magnetic in nature rendering it easily separable and chemical stability at full pH range [13]. Similarly, the layered structure of graphite powder provides high specific surface area for adsorption and its anisotropic nature in terms of layered structure makes it suitable candidate for intercalation of various type of chemical specie [14]. In the present study, the adsorption of Allura red on magnetic iron oxide α-Fe_2O_3 nanoparticles and α-Fe_2O_3/G-p nanocomposite was carried out. Pore size analysis was carried out using BJH model whereas other adsorption isotherm models such as Langmuir, Freundlich, Dubinin-Radushkevich (D-R) and BET were applied to equilibrium adsorption data to reveal nature of adsorption. Kinetic and thermodynamic parameters were also evaluated by applying different kinetic models and thermodynamic equations.

2. Materials and methods

2.1. Materials

Graphite powder (<150 µm, purity 99.99%) was purchased from Sigma Aldrich. Anhydrous salts of iron(II) chloride (purity 99.99%), iron(III) chloride (purity 99.99%), anhydrous sodium hydroxide (purity 99.99%), poly(vinyl alcohol) M_w 89,000–98,000 (purity 99%) and dodecylbenzenesulfonic acid sodium salt were also purchased from Sigma Aldrich. The buffers solution of analytical grade of pH 2, 3, 4, 7, 6, 8 and 10 was purchased from Hannainst.

2.2.Preparation of magnetic iron oxide hematite (α-Fe_2O_3) nanoparticles

The magnetic α-Fe_2O_3 nanoparticles were prepared by co-precipitation method with slight modification [15]. Mixture of Fe^{3+}/Fe^{2+} in molar ratio of 2:1 was prepared in (deionized) D.I water and was heated at 80°C during which 0.01 g polyvinyl alcohol (PVA) was dissolved in mixture through vigorous stirring for 1 h. While maintaining the temperature at 80°C, 1 M NaOH solution was added drop wise through syringe during vigorous stirring for 2 h until the mixture turned black. Finally the black precipitate was washed with D.I water through centrifugation at 4000 rpm (Hettich MIKRO 220) until the pH of supernatant was between 7 and 8. The washed precipitates were dried in an oven at 90°C and finally calcined at 500°C in furnace for 5 h inorder to obtain brown colored magnetic α-Fe_2O_3 nanoparticles [16].

2.3. Preparation of magnetic α-Fe_2O_3/graphite powder (α-Fe_2O_3/G-p) nanocomposite

For the preparation of nanocomposite, the graphite powder was crushed with agate mortar and pestle continuously for 4 h in order to obtain very fine graphite powder (G-p). Then dodecylbenzenesulfonic acid (DBSA) solution was prepared in 250 mL by adding 0.25 g DBSA to D.I water after which 1 g crushed G-p was added followed by ultrasonication for 6 h for the non-covalent functionalization of G-p [17]. The G-p was separated from solution by centrifugation at 6000 rpm (Hettich MIKRO 220) and washed with D.I water to remove excess surfactant followed by drying at 80°C for 4 h. The nanocomposite was prepared only by adding 0.5 g of functionalized G-p to mixture of Fe^{3+}/Fe^{2+} (2:1) in D.I water followed by ultrasonication for 4 h. The rest of the procedure which was followed is same as mentioned in section 2.2.

2.4. Adsorption studies

In order to collect equilibrium, kinetic and thermodynamic data for adsorption, batch technique was applied [18]. Stock solution of Allura red was prepared by dissolving appropriate amount of Allura red in D.I water from which the working standard solutions were prepared by carrying out necessary dilutions. The adsorption process data was collected by using 0.01 g of adsorbent in 10 mL buffered solutions of adsorbate in 15 mL glass vials. Then the shaking of mixtures were carried out in a thermostatic water bath orbital shaker (MaxQ7000) with shaking speed of 100 rpm for 3 h in order to make sure that equilibrium is achieved. The adsorbent was separated from adsorbate by centrifugation at 6000 rpm for 30 min (Hettich MIKRO 220). The supernatant was then analyzed for adsorbate concentration on a UV-visible spectrophotometer at a wavelength of 520 nm [19].

2.5. Desorption study

In order to study the recovery of adsorbents after adsorption for reusability while retaining their adsorptive character, desorption study was conducted. After performing the adsorption experiment, the adsorbents with loaded dye were separated by centrifugation and transferred to 20 mL glass vial containing 0.1 mol/L NaOH aqueous solution followed by stirring for 2 h. After achieving equilibration, the adsorbents were removed by centrifugation and the Allura red dye concentration in supernatant was measured by UV-Vis spectroscopy. The average values were collected after performing adsorption-desorption experiments three times.

2.6. Characterization

The morphology of adsorbents were studied by making use of Scanning electron microscopy (SEM) images which were obtained using a JEOL JSM-6300 after adsorbent aqueous dispersion was dried under vacuum on a glass slide for approximately 3 h at 80°C and coated with gold by sputtering. Wide-angle X-ray diffraction (WAXD) patterns were measured at room temperature using a Theta-Theta instrument with a beam of Cu Kα radiation ($\lambda = 0.15418$ nm) with accelerating voltage and current of 40 kV and 40 mA in order to determine the crystallographic structure. The data were analyzed using the WIN-XPOW and Xpert high score program. Infrared (IR) transmittance spectra were obtained on a Perkin–Elmer SPECTRUM1000 Fourier transform Infra Red (FTIR) spectrophotometer with resolution of 1 cm^{-1} in transmission mode at room temperature. In order to remove the interference from solvent molecules in FTIR spectroscopy, the adsorbents were dried under vacuum at 60°C. The surface area and porosity of adsorbents were analysed by N_2 adsorption at liquid nitrogen temperature (77.350 K) in a Quantachrome NOVA 2200e instrument and the samples were heated in a vacuum oven at 150°C for 5 h under complete vacuum for removal of adsorbed gases (N_2, O_2) prior to analysis. The Allura red dye absorbance was measured using a UV/visible double beam spectrophotometer (Hitachi Model U-2500) at 520 nm which is the maximum adsorption wavelength for Allura red and the concentrations were determined by applying Beer-Lambert law respectively. In order to measure the pH of the point of zero charge pH_{pzc} for the adsorbents, 0.1 g of each α-Fe_2O_3 nanoparticles and α-Fe_2O_3/G-p nanocomposite were introduced into nine vials separately, containing 0.1 M $NaNO_3$ solution. Adjustment of the pH values of vials to 2, 3, 4, 5, 6, 7, 8, 9 and 10 was carried out using solutions of 0.01 mol/L HCl and NH_3. The measurement of final pH was conducted after 24h when equilibration was achieved in a thermostatic water bath orbital shaker (MaxQ7000) with shaking speed of 100 rpm for 24 h.

3. Results and discussion

3.1. Characterization of adsorbents

The morphology of magnetic α-Fe_2O_3 nanoparticles and α-Fe_2O_3/G-p nanocomposite was observed with SEM. The SEM images of magnetic α-Fe_2O_3nanoparticles show the homogeneity with respect to size and shape as shown in Fig. 1a. The particle size is in the range of 20–30 nm whereas some of the particles agglomerates are in micron size. In comparison, the α-Fe_2O_3/G-p nanocomposite images reveal the presence of G-p flakes as well as the magnetic α-Fe_2O_3 nanoparticles grown on its surface which confirms the interaction between G-p and magnetic α-Fe_2O_3 nanoparticles as shown in Fig. 1b. It is also evident from SEM images

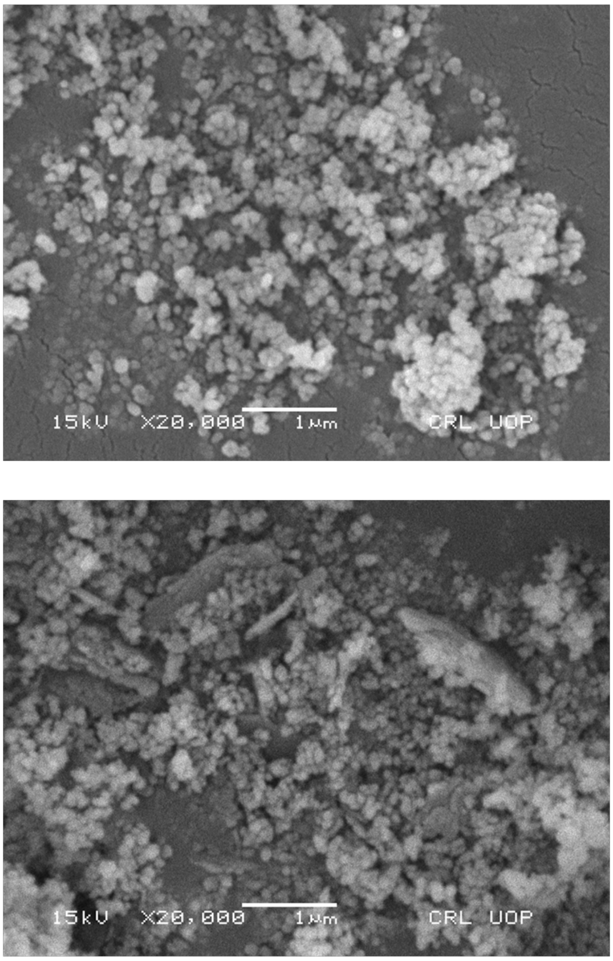

Fig. 1. SEM micrographs of: (a) magnetic α-Fe_2O_3 nanoparticles; (b)α-Fe_2O_3/G-p nanocomposite.

that nanocomposite formation is homogeneous in nature as the G-p has been properly coated with the magnetic α-Fe_2O_3 nanoparticles.

X-ray analysis was performed to affirm the trigonal crystal structure of α-Fe_2O_3 which show typical peaks in XRD pattern located at 2θ = 23.9°, 33.05°, 35.35°, 40.55°, 49.15°, 53.75°, 62.15° and 63.7° assigned to (012), (104), (110), (113), (024), (116), (214) and (300) planes as shown in Fig. 2a [20]. The graphitic peak appears at 26.35° assigned to (002) plane of C=C layers of graphite in XRD pattern of α-Fe_2O_3/G-p nanocomposite. The Scherrer formula was used to calculate the mean particle diameters from the X-ray diffraction pattern according to (104) plane assigned to position 2θ = 33.05° as reference peak;

$$D = \frac{K\lambda}{\beta\, Cos\, \theta} \tag{1}$$

The value of β corresponds to FWHM which was determined by using gaussian function in origin software and the value was converted from angle to radian whereas the wavelength λ of Cu Kα X-ray radiation is 0.15418 nm. The shape factor K value is 0.9 for haematite α-Fe_2O_3. The average crystallite size for the α-Fe_2O_3 nanoparticles and α-Fe_2O_3/G-p nanocomposite was determined to be 31.33 and 33.70 nm respectively [21].

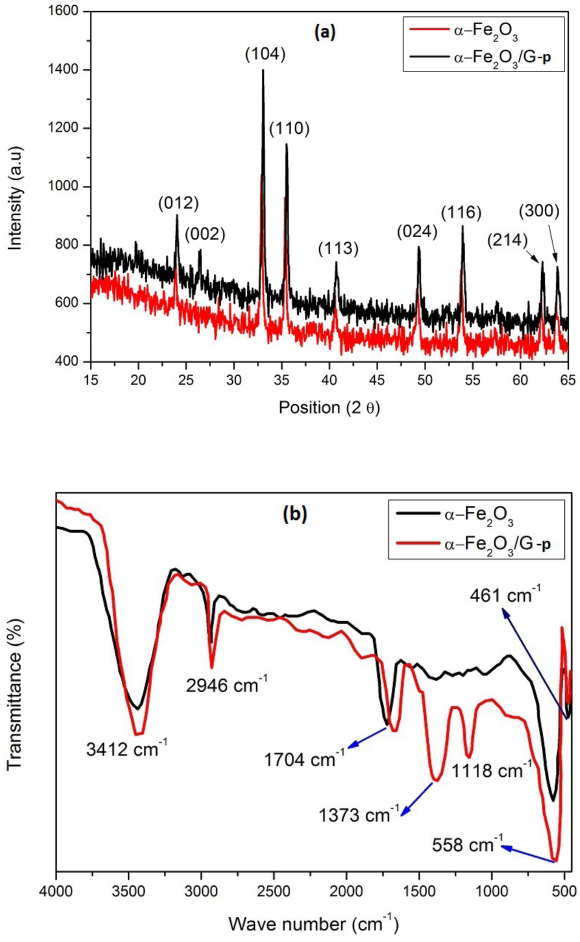

Fig. 2. (a) XRD pattern and (b) FTIR spectrum of magnetic α-Fe_2O_3 nanoparticles and α-Fe_2O_3/G-p nanocomposite.

The IR spectra of α-Fe_2O_3 nanoparticles and α-Fe_2O_3/G-p nanocomposite shows the prominent peaks at 558 and 461 cm^{-1} characteristic of α-Fe_2O_3 nanoparticles which can be assigned to Fe-O intrinsic stretching vibration and bending vibration mode O-Fe-O, respectively as shown in Fig. 2b [22]. Similarly, the appearance of three sharp peaks at 3412, 2946 and 1704 cm^{-1} confirms the presence of physically adsorbed water molecule at surface of products as these peaks corresponds to the asymmetrical stretching vibration and deformation vibrations of −OH group. The π-π interaction among the graphitic walls of G-p gives two peaks at 1118 cm^{-1} and 1373 cm^{-1} respectively. The broad and intense peak at 1627 cm^{-1} corresponds to C=C stretching mode of G-p side wall defects [23]. Both XRD and FTIR results affirm the synthesis of desired product.

Nitrogen adsorption isotherms of α-Fe_2O_3 nanoparticles and α-Fe_2O_3/G-p nanocomposite show that surface adsorption is followed by pore filling phenomena depicting the capillary condensation in porous surface as shown in Figs. 3 and 4. The BET multilayer model applied to nitrogen adsorption isotherms, was used to determine specific surface areas of the adsorbents by linearly fitting the data until maximum recommended limit of $p/p°$ by using the linear form of BET equation;

$$\frac{1}{\left[Q\left(\frac{p^o}{p}-1\right)\right]} = \frac{c-1}{Q_m c}\left(\frac{p}{p^o}\right)+\frac{1}{Q_m c} \tag{2}$$

whereas Q is the adsorbed gas quantity (cm^3/g), Q_m is the monolayer adsorbed gas quantity (cm^3/g), $p/p°$ is the relative pressure and c is the BET constant [24]. There is a prominent increase in the BET surface area of samples as it show a rise from 186.88 m^2/g surface area of α-Fe_2O_3 nanoparticles to 349.85 m^2/g of α-Fe_2O_3/G-p nanocomposite. The porous nature of G-p is main element behind the relative increase in surface area of α-Fe_2O_3/G-p nanocomposite and similarly, the bulky molecules of PVA and DBSA leaves behind pores after calcination at higher temperature.

The statistical thickness of adsorbate on adsorbent is determined by using de-Boer equation which is given as

$$t\left(\dot{A}\right) = \left(\frac{13.99}{\log\left(\frac{p^o}{p}\right)+0.034}\right)^{1/2} \tag{3}$$

whereas t is the statistical thickness ($\dot{A}$) of the adsorbed layer [25]. Then by plotting the adsorbed quantity for each pressure as a function of $t(P)$, *t-plot* is obtained which reveals the nature of surface texture to be porous (non-linear behaviour of *t-plot*) or non-porous (linear behaviour of *t-plot*). It is a known fact that there are two regions prominent in *t-plot* for mesoporous material in which one region preceding the capillary condensation refers to adsorption on internal surfaces of pores along with the external surface whose linear fit slope gives total surface area; whereas after capillary condensation, adsorption is only restricted to external surface on which the slope of linear fit corresponds to

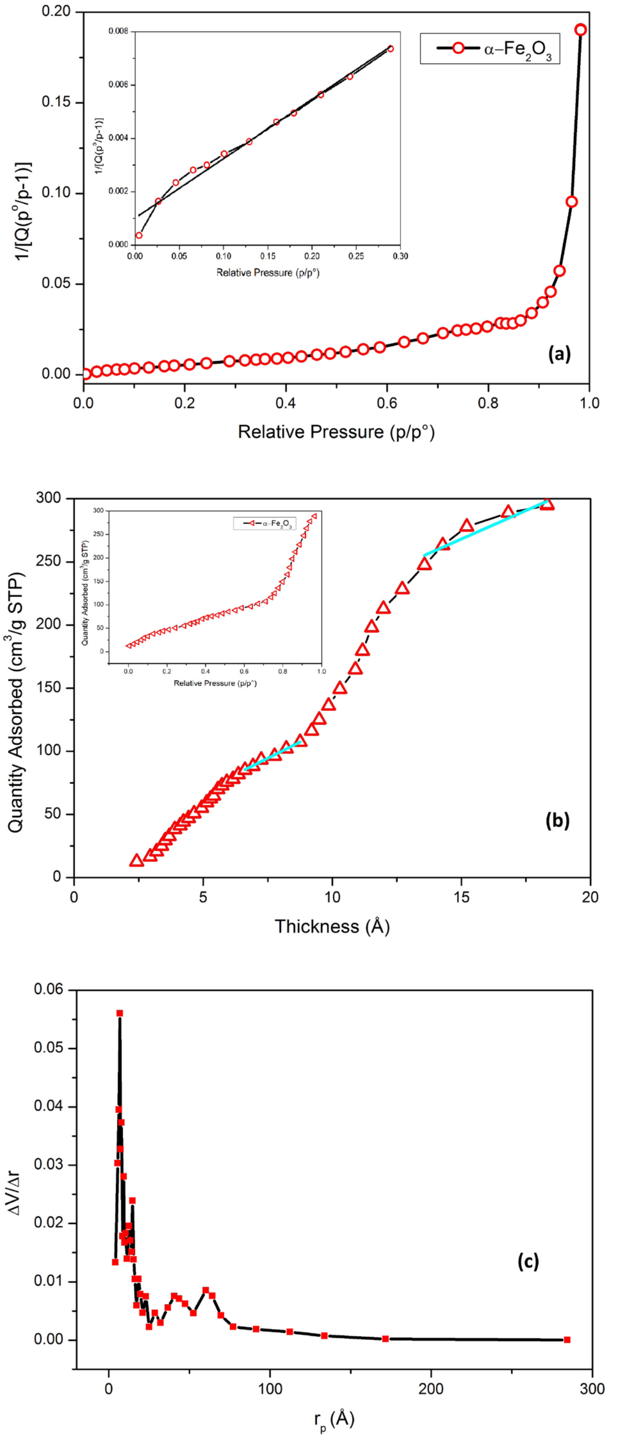

Fig. 3. (a) BET plot for nitrogen adsorption at 77 K with the inset of linear fit for α-Fe_2O_3 nanoparticles; (b) t-plot obtained for nitrogen adsorption at 77 K with inset of nitrogen adsorption isotherm for α-Fe_2O_3 nanoparticles; and (c) pore-size distribution curve for α-Fe_2O_3 nanoparticles.

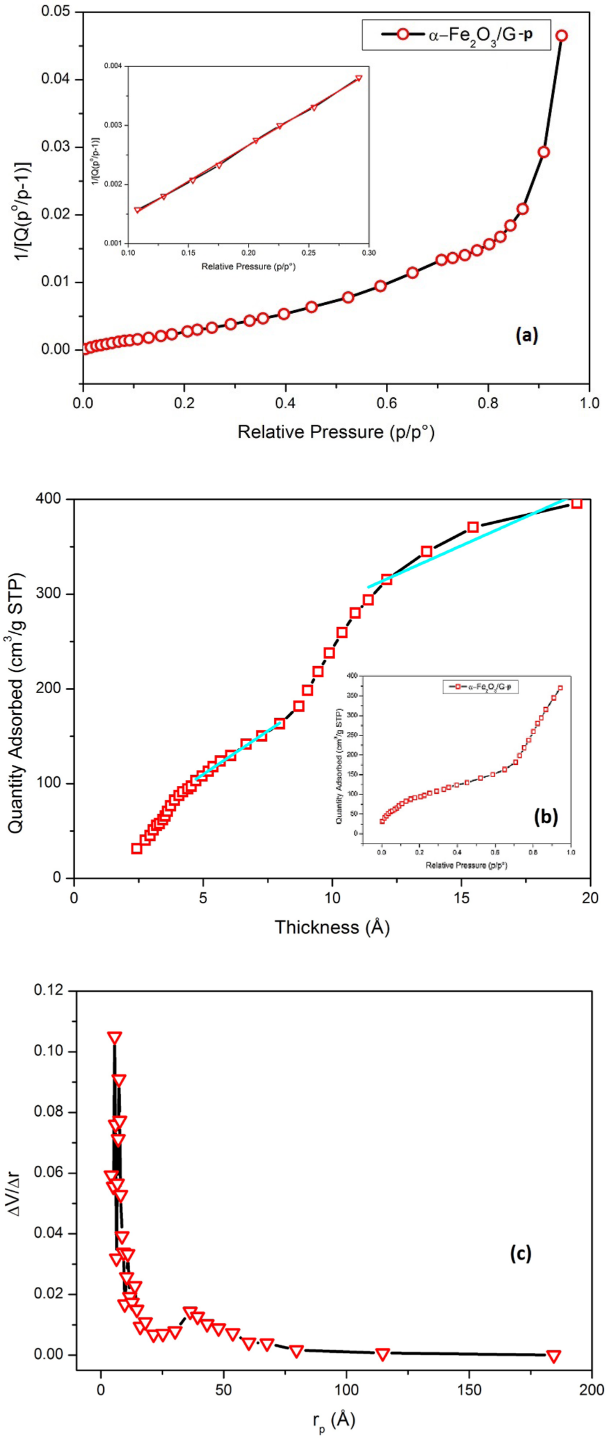

Fig. 4. (a) BET plot for nitrogen adsorption at 77 K with the inset of linear fit for α-Fe_2O_3/G-p nanocomposite; (b) t-plot obtained for nitrogen adsorption at 77 K with inset of nitrogen adsorption isotherm for α-Fe_2O_3/G-p nanocomposite; and (c) pore-size distribution curve for α-Fe_2O_3/G-p nanocomposite.

external surface area and intercept to the mesopore volume respectively. The mesopore volume shows an increase from 0.2056 cm^3/g of α-Fe_2O_3 nanoparticles upto 0.2608 cm^3/g of α-Fe_2O_3/G-p nanocomposite. The subtraction of external surface area from the total surface area will give us mesoporous surface area which is 47.467 m^2/g and 147.142 m^2/g for α-Fe_2O_3 nanoparticles and α-Fe_2O_3/G-p nanocomposite respectively. If the linear fit in the low thickness region, which corresponds to low pressure, doesn't pass through origin, then it should not be confused with the microporosity as mesopore surface show adsorption phenomena similar to non-porous surface if the diameter of mesopores is large [26].

The evaluation of the texture of α-Fe_2O_3 nanoparticles and α-Fe_2O_3/G-p nanocomposite for the complete characterization of porous nature of samples, pore size and pore-size distribution concepts are essential. In the mesopore region, the distribution of pore-size was obtained considering the cylindrical shape $\left(Area\ of\ pore = A_p = \frac{2V_p}{r_p}\right)$ of pores by applying the BJH method to adsorption branch of the nitrogen adsorption isotherms at 77 K and equations for it are given as [27];

$$V_p = R_n \Delta V - R_n c \sum_{j=1}^{n-1} A_{pj} \tag{4}$$

$$R_n = \frac{r_p^2}{\left(r_k + \Delta t\right)^2} \tag{5}$$

$$c = \frac{\left(\overline{r_p} - t_r\right)}{\overline{r_p}} \tag{6}$$

$$log \frac{p}{p^o} = \frac{-4.14}{r_k} \tag{7}$$

where V_p is the volume in pores, ΔV_p is the observed volume of gas desorbed, r_p is the radius of empty pore, r_k is the radius of inner capillary of physically adsorbed layer in pore and t_r is the statistical thickness of adsorbed layer. The range for majority of mesopore diameter lies in between 4 to 25 nm for both α-Fe_2O_3 nanoparticles as well as α-Fe_2O_3/G-p nanocomposite having more than one maximum respectively. The rest of physical characteristics of surface texture determined by BET model and t-plot method are given in Table 1.

The number of negatively charged and positively charged surface sites of adsorbents are equal at certain pH, referred to as the point of surface charge neutrality, known as point of zero charge (pzc) which is basically pH_{pzc} at which the surface charge density is zero and the $pH_{initial}$ is equal to pH_{final} after the removal of adsorbent from solution. For pH values below the pH_{pzc}, the positively charged sites dominate the adsorbents surface whereas it is negatively charged for values above the pH_{pzc}. As shown in Fig. 5a, the pH_{pzc} for α-Fe_2O_3 nanoparticles and α-Fe_2O_3/G-p nanocomposite is 7 and 6 respectively. As a result, the adsorption efficiency of both α-Fe_2O_3nanoparticles and α-Fe_2O_3/G-p nanocomposite decreases with increase in the pH as shown in Fig. 5b which is due to the fact that the attractive electrostatic interaction exist between the positively charged adsorbent surface and negatively charged sulfonate group of the Allura red dye at pH values below pH_{pzc} value, similarly, the repulsive electrostatic interaction will dominate between adsorbate and adsorbent at pH values above pH_{pzc} value [28].

The effects of the variation of adsorbent dosage in the range of 5.0–17.5 mg on the adsorption of Allura red dye having a initial concentration of 25 ppm, was conducted at temperature 30°C and pH 4.0. There is an increase in the adsorption efficiency from 64% to 89% for α-Fe_2O_3 nanoparticles and from 74% to 94% for α-Fe_2O_3/G-p nanocomposite with increase in adsorbent dosage from 5.0 mg to 10.0 mg depicting a pro-

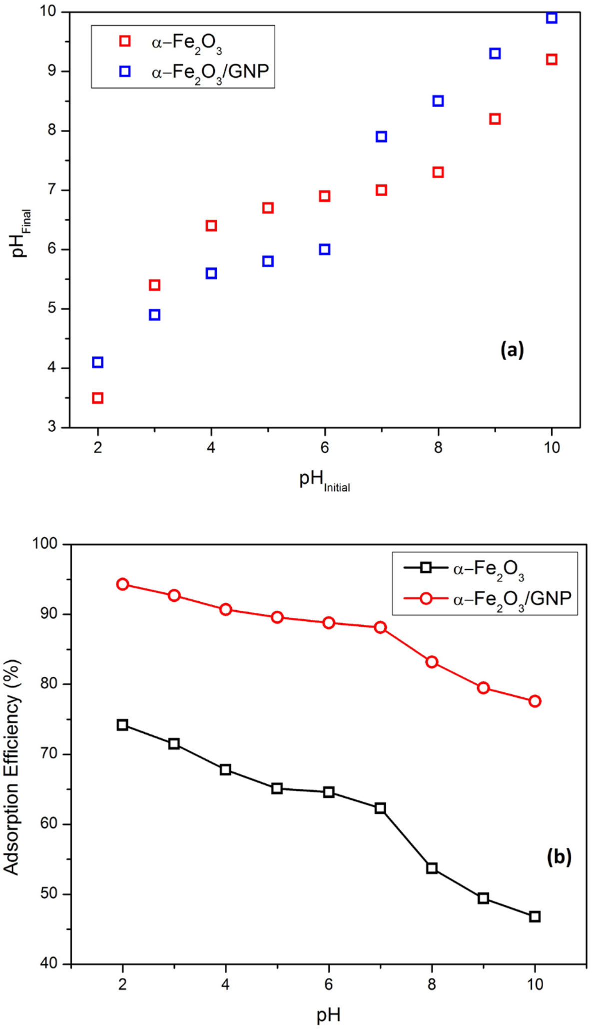

Fig. 5. (a) Measurement of the point of zero charge pH_{pzc} and (b) Effect of pH on the adsorption efficiency for adsorbents.

Table 1
Physical textural properties derived from N_2 adsorption at 77 K on α-Fe_2O_3 nanoparticles and α-Fe_2O_3/G-p nanocomposite

Adsorbents	BET adsorption isotherm model				t-plot method				
	S_{BET} (m^2/g)	c	Q_m	R^2	$V_{Mesopore}$ (cm^3/g)	$S_{Mesopore}$ (m^2/g)	$S_{External}$ (m^2/g)	$S_{t\text{-}plot}$ (m^2/g)	R^2
α-Fe_2O_3	186.88	23.06	42.94	0.955	0.2056	47.46	139.41	0.03	0.883
α-Fe_2O_3/G-p	349.86	56.29	80.38	0.998	0.2608	147.14	188.25	0.02	0.988

found effect of surface area increase on adsorption as shown in Fig. 6a. Further increase in adsorbent dosage from 10.0 mg to 17.5 mg does not produce any significant effect on adsorption efficiency due to which optimum amount of 0.01 g was selected for further adsorption experiments.

Similarly, at 30°C temperature and pH 4.0, the effect of contact time between adsorbate and adsorbent was evaluated using initial concentration of 25 ppm for Allura red dye and the concentration of dye was measured at regular interval 10 min in the range of 10–100 min confirming the equilibration time of 60 min for both the adsorbents for the adsorption process as shown in Fig. 6b. It points to the fact that saturation of active sites on available adsorbent surface is obtained in 60 min and further increase in contact time will not produce any prominent effect on adsorption efficiency.

3.2. Adsorption efficiency

The dynamic equilibrium established for adsorption of Allura red on α-Fe_2O_3 nanoparticles and α-Fe_2O_3/G-p nanocomposite as a function of temperature show equilibration time of 60 min. As complete adsorption of Allura red on α-Fe_2O_3 nanoparticles and α-Fe_2O_3/G-p nanocomposite is achieved in 60 min, it also shows a rapid increase in its removal with increase in temperature as shown in Figs. 7a and b as determined by following expression;

$$\text{Adsorption Efficiency}(\%) = \frac{C_o - C_e}{C_o} \times 100 \tag{8}$$

where C_o and C_e is the initial and equilibrium concentration of adsorbate (mg/L). The increase in adsorption efficiency with increase in temperature is visible in figure which is later confirmed by endothermic adsorption enthalpy change (ΔH), as the adsorbate mobility increases with increase in temperature. The presence of mesoporosity on α-Fe_2O_3 nanoparticles and α-Fe_2O_3/G-p nanocomposite plays a major role in adsorption of Allura red. The adsorption efficiency increased from 62.3% at 303 K to 90.5% at 363 K for α-Fe_2O_3 nanoparticles whereas 88.13% to 97.37% for α-Fe_2O_3/G-p nanocomposite. The increase in adsorption efficiency is attributed to increase in the mesoporous assembly resulting in higher surface area of nanocomposite as compared to nanoparticles because one of the factors

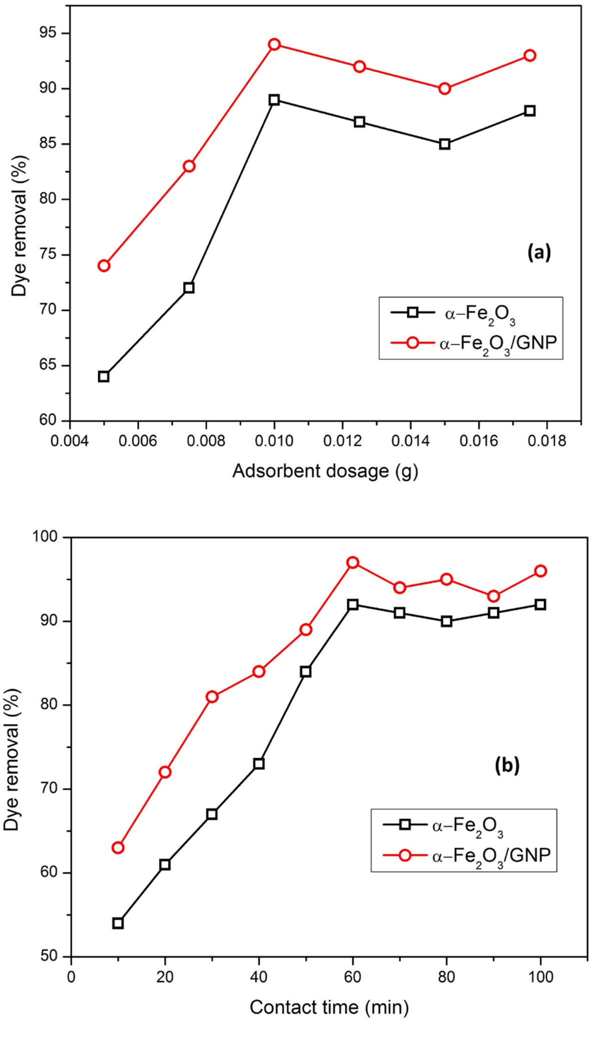

Fig. 6. (a) Effect of adsorbent dosage on adsorption process and (b)effect of contact time on the adsorption efficiency for adsorbents.

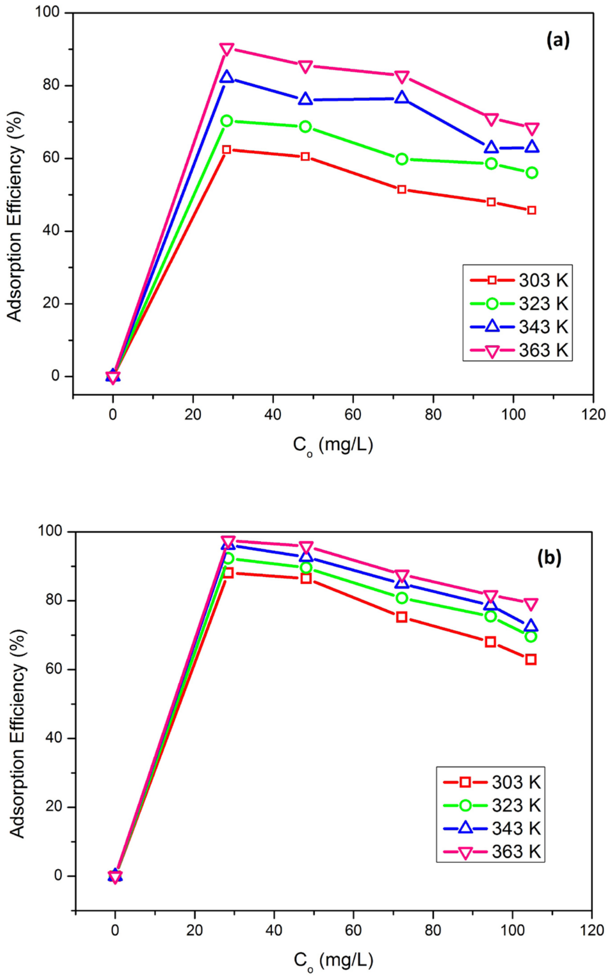

Fig. 7. Adsorption efficiency of Allura red onto the (a) α-Fe_2O_3 nanoparticles; and (b) α-Fe_2O_3/G-p nanocomposite.

on which solute adsorption depends is the surface area of porous adsorbent [29].

3.3. Equilibrium studies

The adsorption isotherm models are applied to the adsorption isotherm data in order to evaluate the relationship between adsorbate and adsorbent at equilibrium for understanding the adsorption behavior during the application process. The adsorption capacity of adsorbent was determined by using following expression;

$$q_e = \frac{(C_o - C_e)V}{m} \tag{9}$$

where q_e is the adsorption capacity of Allura red on adsorbent (mg/g), V is the volume of Allura red solution (L) and m is the mass of adsorbent used (g).

The adsorption isotherms are obtained by plotting q_e versus C_e for the adsorption of Allura red by α-Fe_2O_3 nanoparticles and α-Fe_2O_3/G-p nanocomposite at various temperatures as shown in Figs. 8a and b. It is apparent from the figure that the process of adsorption is quite steady until equilibrium is attained. Also the adsorbent is mesoporous in nature.

Furthermore, the adsorption data is fitted into the different isotherm models such as Langmuir, Freundlich, Dubinin-Radushkevich and BET. The statistical analysis of the linear form of these various isotherm models led us to calculate the important parameters required for adsorption process.

For the case of monolayer adsorption, the maximum adsorption of Allura red on the α-Fe_2O_3 nanoparticles and α-Fe_2O_3/G-p nanocomposite is determined by the semi-empirical Langmuir isotherm using its linear form given as;

$$\frac{C_e}{q_e} = \frac{1}{q_o K} + \frac{C_e}{q_o} \tag{10}$$

where C_e is the solute equilibrium concentration (mg/L), q_e is the equilibrium adsorption capacity (mg/g), K is the Langmuir adsorption coefficient (L/mg) and q_o is the maximum monolayer adsorption capacity of adsorbent (mg/g) [30]. For adsorbent, the maximum capacity of monolayer adsorption was obtained from the slope of plot of C_e/q_e versus C_e where as K was calculated from the intercept as shown in Figs. 9a and b.

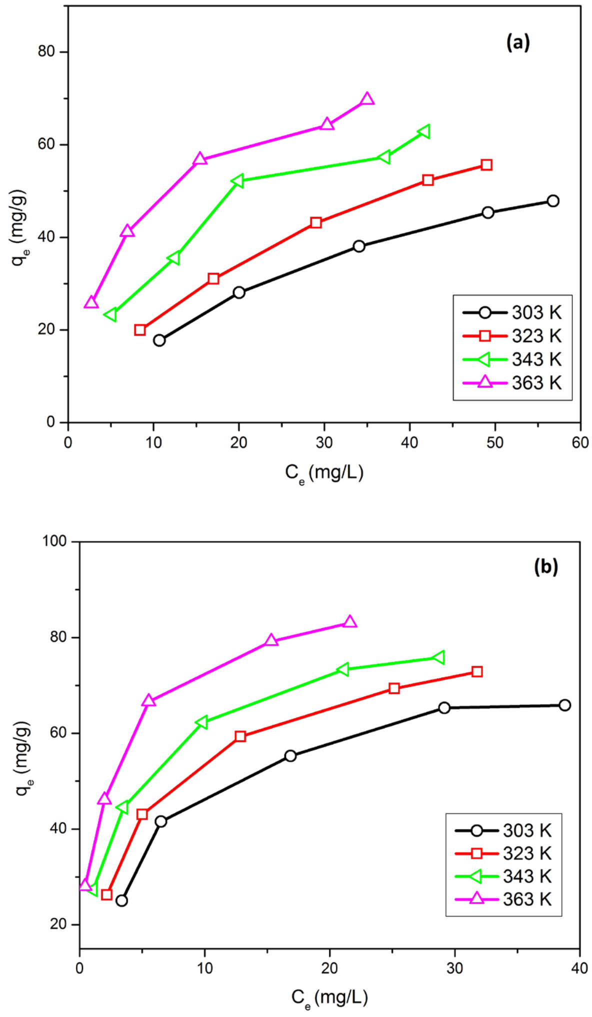

Fig. 8. Adsorption isotherm of Allura Red onto the (a) α-Fe_2O_3 nanoparticles; and (b) α-Fe_2O_3/G-p nanocomposite.

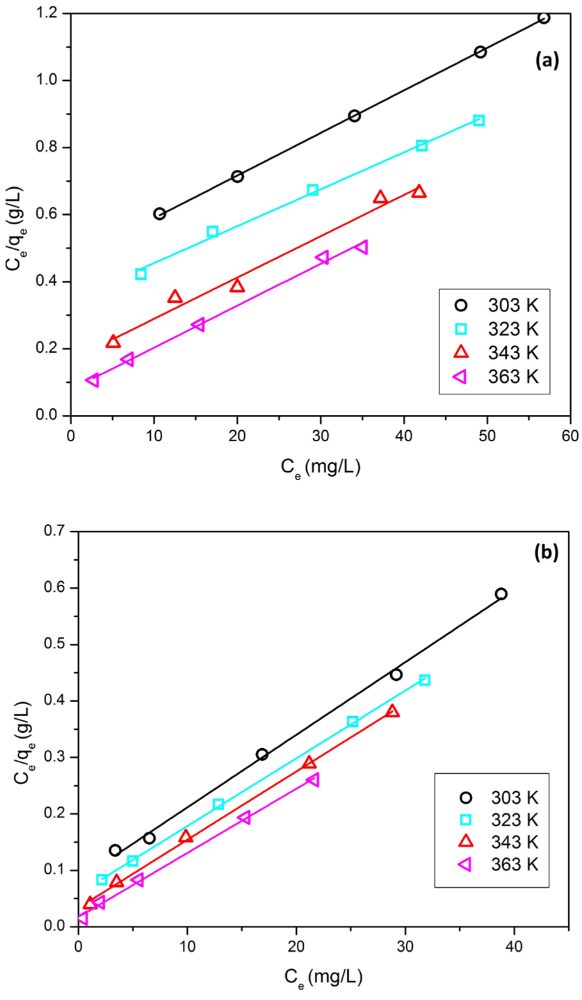

Fig. 9. Experimental data of adsorption isotherm of Allura red on (a) α-Fe_2O_3 nanoparticles; and (b) α-Fe_2O_3/G-p nanocomposite fitted with Langmuir model of adsorption isotherm.

The adsorption data showed linear behavior as it followed the linear equation of Langmuir adsorption isotherm. The maximum monolayer adsorption capacity of adsorbent for Allura red was found to be 79.87 mg/g at 363 K and 87.87 mg/g at 363 K on α-Fe_2O_3 nanoparticles and α-Fe_2O_3/G-p nanocomposite. The high values of correlation coefficients suggest the gradual increase in the adsorption capacity with the increase in equilibrium concentration.

R_L is the dimensionless separation factor value which helps to evaluate the adsorption mechanism i. e., either chemical or physical for the adsorption data following Langmuir adsorption model along with confirmation from thermodynamic calculations. The equation for R_L factor is given as;

$$R_L = \frac{1}{1 + KC_o} \tag{11}$$

The R_L factor values come close to zero with the increase in temperature as given in Table 2, indicating the strengthening of physical interactions between the dyes and the adsorption sites [31]. The range of the R_L values shows the favorable nature of adsorption leading to an increase in maximum monolayer adsorption capacity of adsorbent (mg/g).

For multilayer adsorption of dye on nanoparticles and nanocomposite, Freundlich adsorption isotherm model is applied for understanding the adsorption mechanism [32]. The Freundlich adsorption isotherm equation in its linear form is given as;

$$\ln q_e = \ln K_f + \left(\frac{1}{n}\right)\ln C_e \tag{12}$$

where K_f is the Freundlich constant and *1/n* is the exponent of non-linearity. The constant K_f is obtained from the intercept of linear plot of $\ln q_e$ versus $\ln C_e$ whereas the exponent *1/n* is obtained from the slope as shown in Figs. 10a and b. The constant K_f is indicative of the adsorption capacity at unit concentration (mg/g)/(L/mg)*1/n* whose high values suggest that dye has been adsorbed to greater extent [33]. Similarly, there is a rise in the values of K_f as the temperature increases due to which a gradual increase in q_e value is observed. The intensity of the adsorption is explained by the exponent *1/n* which describes the adsorption by determining the linearity of the plot throughout the range of concentration applied for analysis. The plot will be non-linear curve with *1/n* less than 1 and linear behavior will be observed when *1/n* is equal to 1. For the decrease in the value of *1/n*, the strength of the adsorption bond increases and the adsorption capacity q_e becomes independent of the C_e whereas for larger values of *1/n*, the dependency of q_e increases on C_e due to weakening of the bond between adsorbate and adsorbent. The value of *1/n* for Allura red adsorption on nanocomposite is smaller as compared to nanoparticles indicating more favorable adsorption of Allura red dye on nanocomposite at all temperatures studied [34].

The Dubinin-Radushkevich adsorption isotherm model is expressed in linear form as;

$$\ln q_e = \ln q_m + K'\varepsilon^2 \tag{13}$$

where q_e is the equilibrium adsorption capacity (mg/g), q_m is the maximum monolayer adsorption capacity of adsorbent

Table 2
Adsorption parameters of various adsorption models applied to adsorption data at different temperature on α-Fe_2O_3 nanoparticles and α-Fe_2O_3/G-p nanocomposite

Adsorption isotherm equations	α-Fe_2O_3				α-Fe_2O_3/G-p			
	303K	323K	343K	363K	303K	323K	343K	363K
Langmuir								
q_o *(mg/g)*	78.740	98.827	81.169	79.872	77.700	83.333	82.713	87.874
K (L/mg)	0.0274	0.0319	0.0741	0.16053	0.1554	0.2054	0.3636	0.6742
R^2	0.9997	0.9938	0.9755	0.9952	0.9965	0.9994	0.9985	0.9976
R_L	0.5619	0.5247	0.3219	0.1798	0.1846	0.1462	0.0882	0.0496
Freundlich								
K_f*((mg/g)/(L/mg))*	4.5361	5.7928	11.240	18.680	17.715	21.513	28.342	37.236
1/n	0.5925	0.5878	0.4668	0.3771	0.3826	0.3692	0.3126	0.2810
R^2	0.9868	0.9968	0.9521	0.9667	0.9111	0.9504	0.9692	0.9731
D-R								
q_m *(mg/g)*	44.482	49.957	59.9624	65.653	61.8511	64.906	65.874	69.838
K′ (mol²/kJ²)	19.071	10.725	3.436	1.0113	2.2084	0.9268	0.2636	0.0172
E (kJ/mole)	0.0524	0.0932	0.2910	0.9888	0.4528	1.0789	3.7936	14.007
R^2	0.8968	0.8431	0.7990	0.8454	0.9429	0.8858	0.8141	0.7672
BET								
C	0.02999	-0.0683	2.3512	7.8	20.081	22.167	42.525	7.779
q_x*(cm³/g)*	694.44	-492.61	61.728	58.275	57.43	63.81	73.21	54.55
R^2	0.41416	0.77408	0.11536	0.89991	0.98925	0.98191	0.99461	0.74622

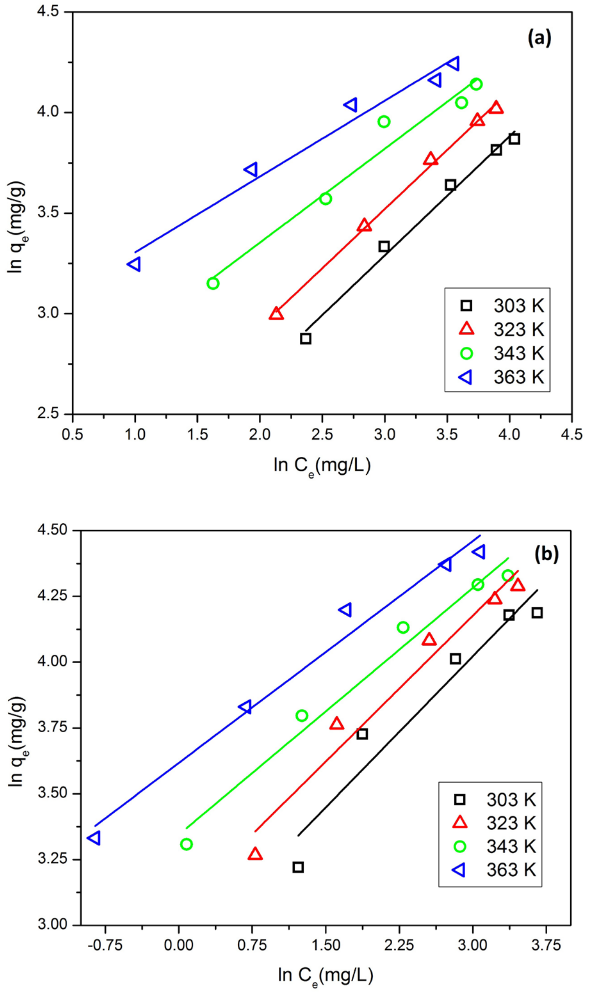

Fig. 10. Experimental data of adsorption isotherm of Allura red on (a) α-Fe_2O_3 nanoparticles; and (b) α-Fe_2O_3/G-p nanocomposite fitted with Freundlich model of adsorption isotherm.

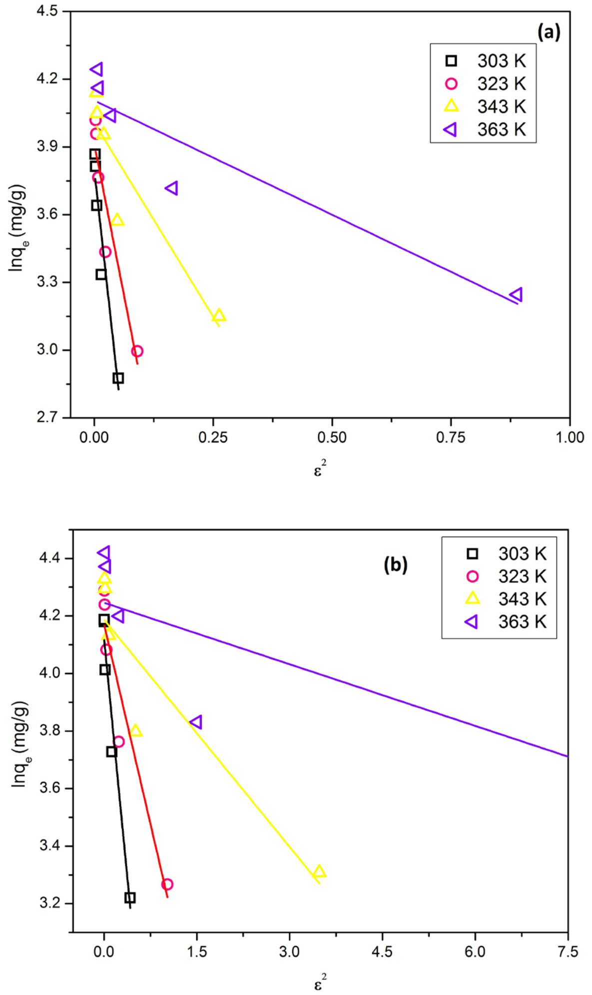

Fig. 11. Experimental data of adsorption isotherm of Allura red on (a) α-Fe_2O_3 nanoparticles; and (b) α-Fe_2O_3/G-p nanocomposite fitted with D-R model of adsorption isotherm.

(mg/g), ε is the Polanyi potential and K' is the adsorption energy constant (mol^2/kJ^2) [35]. The plot of lnq_e versus ε^2 is shown in Figs. 11a and b. The Polanyi potential ε reflects the temperature dependence of adsorption and is expressed as;

$$\varepsilon = RT\ln\left(1+\frac{1}{C_e}\right) \tag{14}$$

where R is universal gas constant, T is the temperature and C_e is the equilibrium concentration (mg/L) of adsorbate. The larger ε value corresponds to better adsorption of adsorbate as favorable adsorption leads to decrease in C_e value. Similarly, the mean adsorption energy E (kJ/mol) gives information regarding the nature of adsorption as physical and chemical and is related to K' as

$$E = \frac{1}{\left(2K'\right)^{\frac{1}{2}}} \tag{15}$$

The value of the mean adsorption energy E less than 8 kJ/mole corresponds to physical adsorption. On the other hand, the value of E in the range of 8–16 kJ/mole points at chemical adsorption [36]. The adsorption of Allura red on α-Fe_2O_3 nanoparticles shows –0.98 kJ/mole value of E whereas α-Fe_2O_3/G-p nanocomposite has E value of –14.01 kJ/mole referring to adsorption phenomena as physical adsorption.

It is important to note that the value of maximum monolayer adsorption capacity determined by Langmuir as q_o is quite different from theoretical monolayer saturation capacity q_m given by D-R because Langmuir isotherm model deals with non-porous homogeneous surface concentrations whereas D-R isotherm model is developed for microporous adsorbents resulting in different approaches for understanding of adsorption mechanism [37].

The BET isotherm model is applied to adsorption processes where multilayer adsorption formation occurs and the linear equation of BET is given as;

$$\frac{C_e/C_o}{q_e\left(1-\frac{C_e}{C_o}\right)} = \frac{1}{q_xC} + \frac{C-1}{q_xC}\frac{C_e}{C_o} \tag{16}$$

where C_o is the initial concentration of adsorbate (mg/g), C_e is equilibrium concentration of adsorbate (mg/L), q_e is

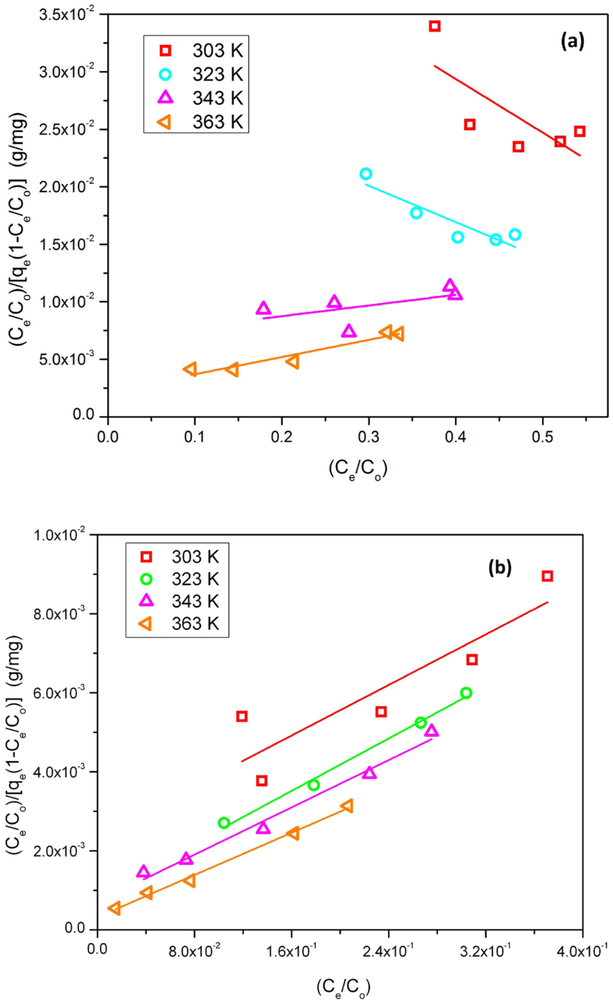

Fig. 12. Experimental data of adsorption isotherm of Allura red on (a) α-Fe_2O_3 nanoparticles; and (b) α-Fe_2O_3/G-p nanocomposite fitted with BET model of adsorption isotherm.

the equilibrium adsorption capacity of adsorbent (mg/g), q_x is the amount of dye required to form monolayer over the surface of adsorbent and C is the parameter related to interaction energy between adsorbent and adsorbate [38]. The linear behavior of the adsorption data as shown in Figs. 12a and b increases with the increase in temperature corresponding to favorable physical multilayer adsorption. Similarly, the value of C is very high for adsorption at higher temperature pertaining to large positive value of adsorption for first layer due to high affinity because of mesoporous nature of the adsorbent [39].

Similarly, the ability of the adsorbent to remove Allura red dye from aqueous solution in this work has been compared with other adsorbents employed for the same purpose as given in Table 3.

3.4. Thermodynamic studies

The integrated form of Van't Hoff equation develops a quantitative relationship of equilibrium constant to the temperature at which it is attained and is expressed as;

Table 3
Comparison of maximum adsorption capacity (q_m) of different adsorbents for Allura red dye

Adsorbent	Maximum monolayer adsorption capacity, q_o (mg/g)	Ref.
Spirulina platensis biomass	503	[40]
Anionic polymeric urethane absorbent (APUA)	90.5	[41]
α-Fe_2O_3 *nanoparticles*	78.74	This work
α-Fe_2O_3*/G-p nanocomposite*	77.70	This work

$$\ln K = \left(\frac{\Delta S}{R}\right) - \left(\frac{\Delta H}{RT}\right) \tag{17}$$

where K is the adsorption equilibrium constant from Langmuir model which is independent of initial concentration C_o, ΔS and ΔH are the changes in entropy and enthalpy which are the two parts of thermodynamic driving force ΔG for the adsorption process given as;

$$-\Delta G = -\Delta H + T\Delta S \tag{18}$$

Similarly, the intrinsic dependency of ΔG on temperature and the concentration of adsorbate are given by the equation as;

$$\Delta G = -RT\ln K \tag{19}$$

Van't Hoff plots are obtained by plotting *ln K* versus *1/T* while ΔS and ΔH are calculated from the intercept and slope as shown in Figs. 13a and b respectively. The negative values of ΔG show that the process of adsorption is feasible and this feasibility is decreasing with the increase in temperature. ΔH shows that the adsorption follows a weak exothermic path as its values are positive (20–40 kJ/mole) and it can be correlated with the R_L factor from Langmuir adsorption model and mean energy of adsorption determined from the D-R model as their relative values indicate that the physical adsorption process is occurring. ΔS shows decrease in the disorder of the adsorbate near adsorbent surface as the values are low and positive [42].

3.5. Kinetic studies

The mechanism of the adsorption phenomenon is evaluated with the kinetic models in order to understand the adsorption phenomenon and determine the ability of the adsorbents for removal of dye. The characteristics of kinetics is essential to be determined for evaluation of adsorption process as several models of kinetics have been designed to describe the dye removal kinetics: (a) a pseudo-first-order kinetic model of Lagergren, (b) a pseudo-second-order kinetic model of Ho, and (c) intra-particle diffusion model of Weber and Morris.

First, the kinetics of liquid-solid phase adsorption was analyzed by the Lagergren pseudo-first-order model equa-

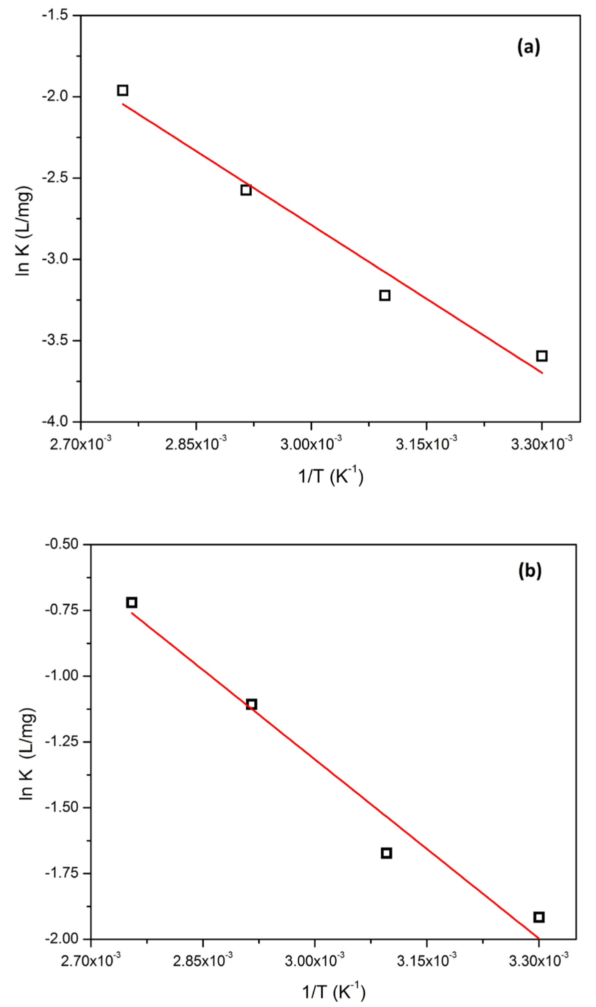

Fig. 13. Linear plot of Van't Hoff for the adsorption of Allura red on (a) α-Fe_2O_3 nanoparticles; and (b) α-Fe_2O_3/G-p nanocomposite.

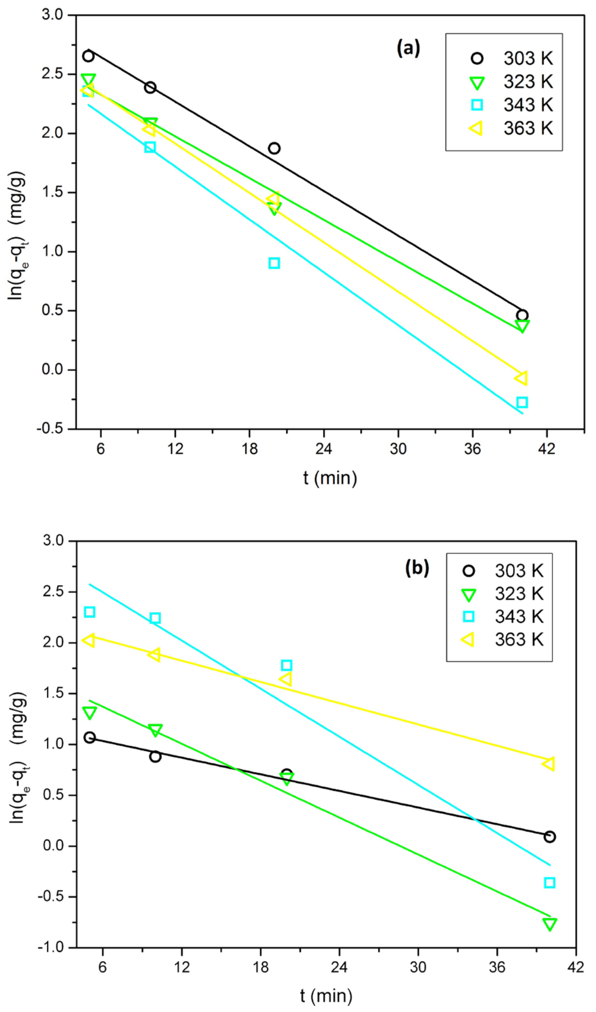

Fig. 14. Pseudo-first order kinetics at different temperature of Allura red on (a) α-Fe_2O_3 nanoparticles; and (b) α-Fe_2O_3/G-p nanocomposite.

tion which is based on adsorbent adsorption capacity given in linear form as

$$\ln(q_e - q_t) = \ln q_e - k_1 t \tag{20}$$

$$q_t = \frac{(C_o - C_t)V}{m} \tag{21}$$

where q_e and q_t are the amounts of solute adsorbed *(mg/g)* at equilibrium and at time *t (min)*, respectively, and k_1 *(1/min)* is the rate constant adsorption. The plots of $ln(q_e - q_t)$ versus *t* at each temperature gave its value of k_1 in the form of slope as calculated by applying model on empirical data as shown in Figs. 14a and b [43]. It is obvious from Table 4 that the mismatch between the experimental $q_{e,exp}$ values with the calculated $q_{e,cal}$ values after applying the linear form of pseudo first order model indicates that this model is not followed by dye adsorption by α-Fe_2O_3 nanoparticles and α-Fe_2O_3/G-p nanocomposite. As q_e is the amount of solute required for full coverage of adsorbent surface at equilibrium, the difference between its experimental and calculated value suggests that the pseudo-first-order kinetics does not consider the solvents interaction with the adsorbate. The rate constant adsorption k_1 *(1/min)* is the oversimplified parameter because it describes the adsorption as single step process. It is also quite visible that with the increase in temperature, the deviation from pseudo first order kinetics becomes greater [44].

The pseudo-second-order kinetic model based on solid phase sorption was also applied to kinetics data of adsorption of Allura red on α-Fe_2O_3 nanoparticles as well as α-Fe_2O_3/G-p nanocomposite and the linear form of the equation is given in the following form as:

$$\frac{t}{q_t} = \frac{1}{k_2 q_e^2} + \frac{t}{q_e} \tag{22}$$

where pseudo-second-order reaction rate constant is k_2 *(g/mg min)*, q_e and q_t are the amounts of solute adsorbed *(mg/g)* at equilibrium and at time *t (min)*, respectively [45]. The plots of t/q_t versus *t* gives straight line for each temperature

Table 4
Thermodynamic parameters derived from Van't Hoff equation for Allura red adsorption on α-Fe_2O_3 nanoparticles and α-Fe_2O_3/G-p nanocomposite

Adsorbent	*T (K)*	*K*	ΔG (kJ/mole)	ΔH (kJ/mole)	ΔS (kJ/mole)	R^2
α-Fe_2O_3	303	0.02743277	–9.05888	25.1771	0.0523	0.96183
	323	0.03987516	–8.65243			
	343	0.07613648	–7.34378			
	363	0.1405334	–5.92222			
α-Fe_2O_3/G-p	303	0.147187	–4.82681	18.8549	0.04562	0.95272
	323	0.187744	–4.49184			
	343	0.330487	–3.15737			
	363	0.486327	–2.17558			

as shown in Figs. 15a and b, from which the pseudo-second-order kinetic constants are calculated and compared with the experimental values as given in Table 5. Also, the initial sorption rate is;

$$k_o = k_2 q_e^2 \tag{23}$$

The values of correlation factor R^2 is greater than 0.99 for each temperature and the q_e is calculated from the linear regression applied to pseudo-second-order model. As compared to pseudo-first-order and intra particle diffusion models, the correlation factor R^2 is very high for pseudo-second-order and there was also good agreement between the experimental $q_{e,exp}$ and the calculated $q_{e,cal}$ values. These resulting values are proof that the adsorption of Allura red on α-Fe_2O_3 nanoparticles as well as α-Fe_2O_3/G-p nanocomposite follows second order kinetics. The rate constants k_2 were found as 0.0013 and 0.0452 g/mg min for α-Fe_2O_3 nanoparticles and α-Fe_2O_3/G-p nanocomposite at 303 K. The adsorption capacity is prominently affected by initial adsorbate concentration and the nature of adsorbent which contribute to difference in the value of experimental and calculated of adsorption capacity [46].

The overall adsorption process of liquid onto solid phase is a multi step process and is controlled by one of the limiting steps which may include film or external diffusion, pore diffusion, surface diffusion and adsorption on the pore surface or a combination of more than one step [43].

The linear equation of intra-particle diffusion model is expressed as:

$$q_t = k_i t^{\frac{1}{2}} + c \tag{24}$$

where k_i is the intra-particle diffusion rate constant (mg/g $min^{1/2}$) and c is the intercept [47]. The porous nature of adsorbent makes it possible to expand the diffusion phenomenon from surface to bulk. Thus, the adsorption which occurs at the outer non-porous surface of the adsorbents is usually followed by much slower process of intra-porous diffusion of the adsorbate into the adsorbents. The intra-particle transport has a rate constant (k_i) in this model which is obtained by plotting a graph of q_t versus $t^{1/2}$ as shown in Figs. 16a and b, which if gives a straight line will lead us to assumption that the prime mechanism is adsorbate diffusion. It can be seen in figure that both plot showed linear behavior indicating that there is no variation in the mass transfer rate in the initial and final stages of adsorption which is responsible for this deviation i.e., the process occurs in two major steps. Initially an external surface adsorption takes place followed by gradual

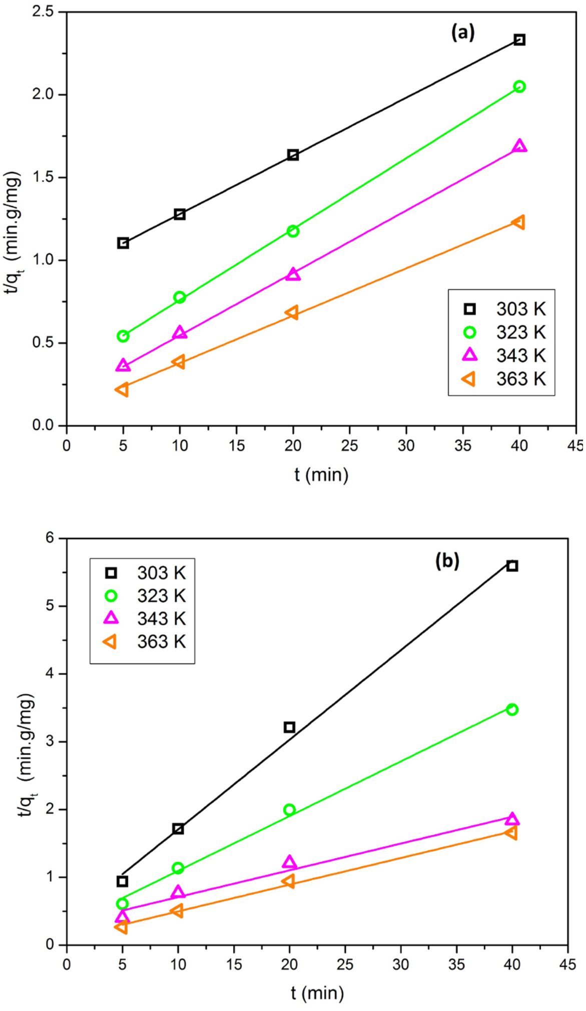

Fig. 15. Pseudo-second-order kinetics at different temperature of Allura red on (a) α-Fe_2O_3 nanoparticles; and (b) α-Fe_2O_3/GNP nanocomposite.

Table 5
Comparison of kinetic models pseudo-first-order of Lagergren, pseudo-second-order of Ho and intra-particle diffusion model of Weber and Morris for Allura red adsorption onα-Fe_2O_3 nanoparticles and α-Fe_2O_3/G-p nanocomposite

Adsorption kinetic models						
Pseudo-first-order kinetic model		$q_{e,exp}$ *(mg/g)*	$q_{e,cal}$ *(mg/g)*	k_1 *(1/min)*		R^2
	α-Fe_2O_3	17.16	20.59359	0.063		0.99112
	α-Fe_2O_3/G-p	7.38	3.309874	0.02726		0.9864
Pseudo-second-order kinetic model		$q_{e,exp}$ *(mg/g)*	$q_{e,cal}$ *(mg/g)*	k_2 *(g/mg.min)*	k_o *(g/mg·min)*	R^2
	α-Fe_2O_3	17.16	28.4576	0.00133	1.077331	0.99994
	α-Fe_2O_3/G-p	7.38	7.565441	0.045215	2.587925	0.9993
Intra-particle diffusion model		$q_{e,exp}$ *(mg/g)*	$q_{e,cal}$ *(mg/g)*	k_i *(mg/g·min)*	*C (mg/g)*	R^2
	α-Fe_2O_3	17.16	18.75	0.30414	0.35579	0.97384
	α-Fe_2O_3/G-p	7.38	8.94	0.43154	4.38804	0.9859

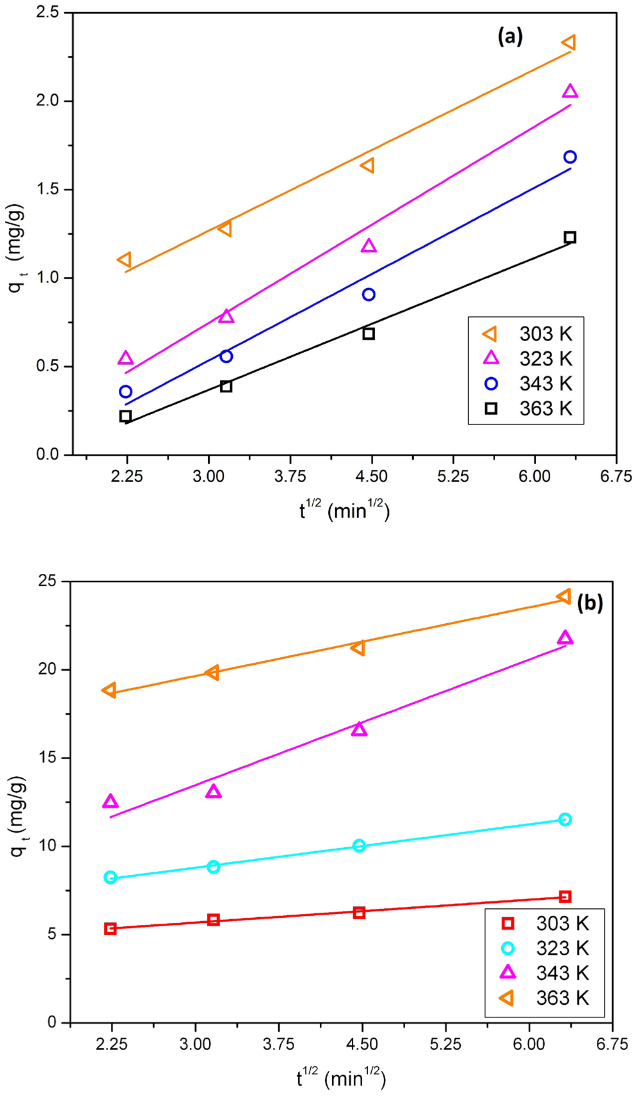

Fig. 16. Intra-particle diffusion kinetics at different temperature of Allura red on (a) α-Fe_2O_3 nanoparticles; and (b) α-Fe_2O_3/G-p nanocomposite.

adsorption process of intra-particle diffusion, until equilibrium is reached [48]. There are several factors which control the rate of adsorption which include the adsorbate molecule size, the adsorbate concentration, the adsorbent surface area, the adsorbent's pore-size distribution and compatibility between adsorbate and adsorbent, the adsorbate bulk phase diffusion coefficient and the level of mixing [49]. The values of R^2 which are calculated from the linear plots of intra-particle diffusion model of kinetics are less as compared to that of the pseudo-second-order reaction which is indicative of fact that the intra-particle diffusion model holds its place in adsorption kinetics only in the beginning of process.

3.6. Activation energy:

The relationship of rate constant to temperature is given by Arrhenius equation as shown in following expression;

$$k = Aexp\left(-\frac{E_a}{RT}\right) \tag{25}$$

where k is the rate constant of sorption (g/mg min), A is the Arrhenius constant (g/mg min), E_a is the activation energy (kJ/mole), R is the universal gas constant (8.314 J/mole) and T is the solution temperature (K) [50].

The linear form of the equation is applied to find the value of energy of activation given as

$$\ln k = \ln A - \frac{E_a}{RT} \tag{26}$$

The plot of ln k vs $1/T$ gives us a straight line as shown in Figs. 17a and b whose slope gives us the energy of activation whose low values point at physical interaction between adsorbate and adsorbent rather than an activated chemical process. The decrease in E_a is more prominent for α-Fe_2O_3/G-p nanocomposite as compared to α-Fe_2O_3 nanoparticles indicating the more favourability of adsorption on α-Fe_2O_3/G-p nanocomposite.

3.7. Desorption

For the purpose of adsorbents regeneration, alkaline solution of NaOH is applied as eluent because the

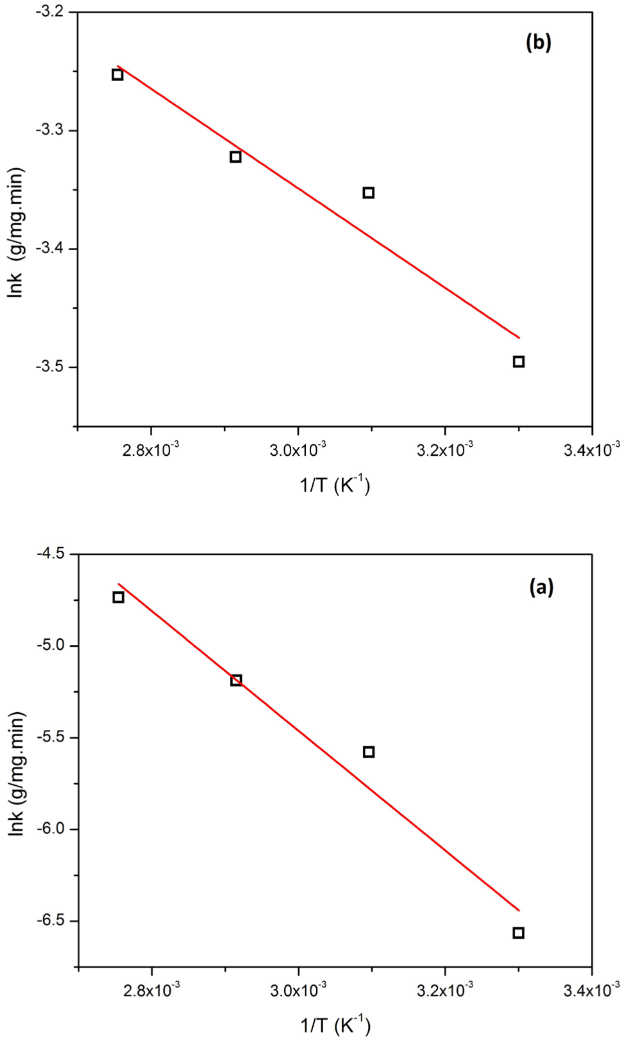

Fig. 17. Activation energy plot for adsorption of Allura red on on (a) α-Fe_2O_3 nanoparticles; and (b) α-Fe_2O_3/G-p nanocomposite.

Table 6
Comparison of Arrhenius constant *A* and activation energy E_a of Arrhenius equation applied to kinetic data of α-Fe_2O_3 nanoparticles and α-Fe_2O_3/G-p nanocomposite

	A (g/mg min)	E_a (kJ/mole)
α-Fe_2O_3	75.63	27.12
α-Fe_2O_3/G-p	3.49	0.12

Table 7
Comparison of desorption of Allura Red dye from loaded α-Fe_2O_3 nanoparticles and α-Fe_2O_3/G-p nanocomposite using 0.1 mol/L NaOH aqueous solution as eluent

Allura red added (µg added)	Allura red added (µg eluted) (α-Fe_2O_3)	Desorption %	Allura red added (µg eluted) (α-Fe_2O_3/G-p)	Desorption %
200	194.46	97.23	198.46	99.23
400	387.28	96.82	394.88	98.72
600	578.76	96.46	584.16	97.36

increase in pH will reduce the interaction between adsorbate and adsorbent due to the anionic nature of Allura red dye as shown in Figs. 5a and b which elaborate the effect of pH on Allura red dye adsorption. Therefore, the increase in pH would make possible the desorption process to occur. The data given in Table 7 confirms that desorption of Allura red dye adsorbed on α-Fe_2O_3/G-p was from 97.23% to 96.46% whereas for α-Fe_2O_3/G-p nanocomposite, it was from 99.23% to 97.36% when 0.1 mol/L NaOH solution was used as eluent confirming pH dependent behavior of desorption process. Comparative results for desorption of janus green dye from oxidized multiwalled carbon nanotubes and methylene blue from brown macroalga were obtained by Sobhanardakani et al. [51] and Daneshvar et al. [52].

4. Conclusion

The increase in the mesoporosity is accompanied by increase in the adsorption efficiency as it is apparent in surface analysis by BET, *t*-plot and BJH method. As α-Fe_2O_3/G-p nanocomposite surface area increases more compared to α-Fe_2O_3 nanoparticles, which is the fact that the adsorption efficiency of α-Fe_2O_3/G-p nanocomposite is greater than α-Fe_2O_3 nanoparticles at all studied temperature and solution concentration. Similarly, there is a rise in adsorption efficiency with rise in temperature showing equilibration time of 60 min. Kinetics study revealed that the kinetics data of sorption processes were best fitted by a pseudo-second-order kinetic model describing its parameters up to mark and kinetics two step mechanism was also well explained by well fitted intra-particle diffusion model suggesting that there is no controlling step. The low activation energy of sorption for α-Fe_2O_3 and α-Fe_2O_3/G-p nanocomposite points at occurrence of physical adsorption process respectively. Langmuir, Freundlich, Dubinin-Radushkevich (D–R), BET isotherm models were linearly fitted to the empirical data. The best fit model was Langmuir isotherm model for both α-Fe_2O_3 nanoparticles and α-Fe_2O_3/G-p nanocomposite and it showed the endothermic nature of adsorption. R_L separation factor for Langmuir and the *1/n* value for Freundlich isotherm confirm that Allura red is quite adequately adsorbed by both α-Fe_2O_3 nanoparticles as well as α-Fe_2O_3/G-p nanocomposite. The adsorption process of Allura red onto α-Fe_2O_3 nanoparticles and α-Fe_2O_3/G-p nanocomposite was spontaneous as is confirmed by negative value of ΔG and positive value of ΔS. The endothermic nature of adsorption was more feasibly explained by positive value of ΔH.

References

[1] K.S. Minioti, C.F. Sakellariou, N.S. Thomaidis, Determination of 13 synthetic food colorants in water-soluble foods by reversed-phase high-performance liquid chromatography coupled with diode-array detector, Anal. Chim. Acta, 583 (2007) 103–110.

[2] A. Bianco Prevot, C. Baiocchi, M.C. Brussino, E. Pramauro, P. Savarino, V. Augugliaro, G. Marci, L. Palmisano, Photocatalytic degradation of acid blue 80 in aqueous solutions containing TiO_2 suspensions, Environ. Sci. Technol., 35 (2001) 971–976.

[3] T.S. Jamil, M.Y. Ghaly, N.A. Fathy, T.A. Abd el-Halim, L. Österlund, Enhancement of TiO_2 behavior on photocatalytic oxidation of MO dye using TiO_2/AC under visible irradiation and sunlight radiation, Sep. Purif. Technol., 98 (2012) 270–279.

[4] A. Pandey, P. Singh, L. Iyengar, Bacterial decolorization and degradation of azo dyes, Int. Biodeter. Biodegr., 59 (2007) 73–84.

[5] T. Sauer, G.C. Neto, H. Jose, R. Moreira, Kinetics of photocatalytic degradation of reactive dyes in a TiO_2 slurry reactor, J. Photochem. Photobio. A: Chem., 149 (2002) 147–154.

[6] S.S. Ashraf, M.A. Rauf, S. Alhadrami, Degradation of Methyl Red using Fenton's reagent and the effect of various salts, Dyes Pigments, 69 (2006) 74–78.

[7] E. Forgacs, T. Cserhati, G. Oros, Removal of synthetic dyes from wastewaters: a review, Environ. Int., 30 (2004) 953–971.

[8] A. Sharma, G. Sharma, M. Naushad, A.A. Ghfar, D. Pathania, Remediation of anionic dye from aqueous system using bio-adsorbent prepared by microwave activation, Environ. Technol., 39 (2018) 917–930.

[9] A.B. Albadarin, M.N. Collins, M. Naushad, S. Shirazian, G. Walker, C. Mangwandi, Activated lignin-chitosan extruded blends for efficient adsorption of methylene blue, Chem. Eng. J., 307 (2017) 264–272.

[10] M. Naushad, Z. Abdullah A.L. Othman, M. Rabiul Awual, S.M. Alfadul, T. Ahamad, Adsorption of rose Bengal dye from aqueous solution by amberlite Ira-938 resin: kinetics, isotherms, and thermodynamic studies, Desal. Water Treat., 57 (2016) 13527–13533.

[11] T.A. Khan, M. Nazir, Enhanced adsorptive removal of a model acid dye bromothymol blue from aqueous solution using magnetic chitosan-bamboo sawdust composite: Batch and column studies, Environ. Prog. Sustain., 34 (2015) 1444–1454.

[12] T.A. Khan, M. Nazir, E.A. Khan, Magnetically modified multiwalled carbon nanotubes for the adsorption of bismarck brown R and Cd (II) from aqueous solution: batch and column studies, Desal. Water Treat., 57 (2016) 19374–19390.

[13] A.A. Alqadami, M. Naushad, M.A. Abdalla, M.R. Khan, Z.A. Alothman, Adsorptive removal of toxic dye using Fe_3O_4–TSC nanocomposite: equilibrium, kinetic, and thermodynamic studies, J. Chem. Eng. Data, 61 (2016) 3806–3813.

[14] M. Caragiu, S. Finberg, Alkali metal adsorption on graphite: a review, J. Phys: Condens. Mat., 17 (2005) R995.

[15] K. Petcharoen, A. Sirivat, Synthesis and characterization of magnetite nanoparticles via the chemical co-precipitation method, Mater. Sci. Eng.: B, 177 (2012) 421–427.

[16] Y. El Mendili, J.-F.o. Bardeau, N. Randrianantoandro, F. Grasset, J.-M. Greneche, Insights into the mechanism related to the phase transition from γ-Fe_2O_3 to α-Fe_2O_3 nanoparticles induced by thermal treatment and laser irradiation, J. Phys. Chem. C, 116 (2012) 23785–23792.

[17] C.Y. Hu, Y.J. Xu, S.W. Duo, R.F. Zhang, M.S. Li, Non-covalent functionalization of carbon nanotubes with surfactants and polymers, J. Chin. Chem. Soc., 56 (2009) 234–239.

[18] E.A. Khan, T.A. Khan, Adsorption of methyl red on activated carbon derived from custard apple (Annona squamosa) fruit shell: Equilibrium isotherm and kinetic studies, J. Mol. Liq., 249 (2018) 1195–1211.

[19] A.R. Kul, H. Koyuncu, Adsorption of Pb (II) ions from aqueous solution by native and activated bentonite: kinetic, equilibrium and thermodynamic study, J. Hazard. Mater., 179 (2010) 332–339.

[20] L. Hu, A. Percheron, D. Chaumont, C.-H. Brachais, Microwave-assisted one-step hydrothermal synthesis of pure iron oxide nanoparticles: magnetite, maghemite and hematite, J. Sol-Gel Sci. Technol., 60 (2011) 198.

[21] H.P. Klug, L.E. Alexander, X-Ray Diffraction Procedures, Wiley, New York, 1954.

[22] I. Chernyshova, M. Hochella Jr, A. Madden, Size-dependent structural transformations of hematite nanoparticles. 1. Phase transition, Phys. Chem. Chem. Phys., 9 (2007) 1736–1750.

[23] Y. Wang, Z. Iqbal, S. Mitra, Rapidly functionalized, water-dispersed carbon nanotubes at high concentration, J. Am. Chem. Soc., 128 (2006) 95–99.

[24] S. Brunauer, P.H. Emmett, E. Teller, Adsorption of gases in multimolecular layers, J. Am. Chem. Soc., 60 (1938) 309–319.

[25] B.C. Lippens, J. De Boer, Studies on pore systems in catalysts: V. The t method, J. Catal., 4 (1965) 319–323.

[26] A. Galarneau, F.o. Villemot, J. Rodriguez, F.o. Fajula, B. Coasne, Validity of the t-plot method to assess microporosity in hierarchical micro/mesoporous materials, Langmuir, 30 (2014) 13266–13274.

[27] E.P. Barrett, L.G. Joyner, P.P. Halenda, The determination of pore volume and area distributions in porous substances. I. Computations from nitrogen isotherms, J. Am. Chem. Soc., 73 (1951) 373–380.

[28] R. Zandipak, S. Sobhanardakani, Synthesis of $NiFe_2O_4$ nanoparticles for removal of anionic dyes from aqueous solution, Desal. Water Treat., 57 (2016) 11348–11360.

[29] T.-H. Liou, Development of mesoporous structure and high adsorption capacity of biomass-based activated carbon by phosphoric acid and zinc chloride activation, Chem. Eng. J., 158 (2010) 129–142.

[30] G. Belton, Langmuir adsorption, the Gibbs adsorption isotherm, and interracial kinetics in liquid metal systems, Metal. Transac. B, 7 (1976) 35–42.

[31] M. Greluk, Z. Hubicki, Kinetics, isotherm and thermodynamic studies of Reactive Black 5 removal by acid acrylic resins, Chem. Eng. J., 162 (2010) 919–926.

[32] J. Appel, Freundlich's adsorption isotherm, Surf. Sci., 39 (1973) 237–244.

[33] G. Crini, P.-M. Badot, Application of chitosan, a natural aminopolysaccharide, for dye removal from aqueous solutions by adsorption processes using batch studies: a review of recent literature, Prog. Polym. Sci., 33 (2008) 399–447.

[34] B. Hameed, A. Ahmad, K. Latiff, Adsorption of basic dye (methylene blue) onto activated carbon prepared from rattan sawdust, Dyes Pigments, 75 (2007) 143–149.

[35] K. Foo, B.H. Hameed, Insights into the modeling of adsorption isotherm systems, Chem. Eng. J., 156 (2010) 2–10.

[36] E.R. Monazam, L.J. Shadle, D.C. Miller, H.W. Pennline, D.J. Fauth, J.S. Hoffman, M.L. Gray, Equilibrium and kinetics analysis of carbon dioxide capture using immobilized amine on a mesoporous silica, AIChE J., 59 (2013) 923–935.

[37] N.D. Hutson, R.T. Yang, Theoretical basis for the Dubinin-Radushkevitch (DR) adsorption isotherm equation, Adsorption, 3 (1997) 189–195.

[38] A. Ebadi, J.S.S. Mohammadzadeh, A. Khudiev, What is the correct form of BET isotherm for modeling liquid phase adsorption?, Adsorption, 15 (2009) 65–73.

[39] W.J. Weber, Physicochemical Processes for Water Quality Control, Wiley Interscience, New York, 1972.

[40] G.L. Dotto, M.L.G. Vieira, V.M. Esquerdo, L.A.A. Pinto, Equilibrium and thermodynamics of azo dyes biosorption onto Spirulina platensis, Braz. J. Chem. Eng., 30 (2013) 13–21.

[41] A. Pirkarami, M.E. Olya, F. Najafi, Removal of azo dye from aqueous solution using an anionic polymeric urethane absorbent (APUA), J. Ind. Eng. Chem., 21 (2015) 387–393.

[42] W.J. Moore, Basic Physical Chemistry, Prentice Hall, New Jersey, 1983.

[43] Y.-S. Ho, G. McKay, Pseudo-second order model for sorption processes, Process Biochem., 34 (1999) 451–465.

[44] H. Yuh-Shan, Citation review of Lagergren kinetic rate equation on adsorption reactions, Scientometrics, 59 (2004) 171–177.

[45] Y.-S. Ho, Review of second-order models for adsorption systems, J. Hazard. Mater., 136 (2006) 681–689.

[46] Y.-S. Ho, G. McKay, The kinetics of sorption of divalent metal ions onto sphagnum moss peat, Water Res., 34 (2000) 735–742.

[47] F.-C. Wu, R.-L. Tseng, R.-S. Juang, Initial behavior of intraparticle diffusion model used in the description of adsorption kinetics, Chem. Eng. J., 153 (2009) 1–8.

[48] W. Cheung, Y. Szeto, G. McKay, Intraparticle diffusion processes during acid dye adsorption onto chitosan, Bioresour. Technol., 98 (2007) 2897–2904.

[49] A.W. Adamson, A.P. Gast, Physical Chemistry of Surfaces, Los Angeles, 1967.

[50] M. Doğan, H. Abak, M. Alkan, Adsorption of methylene blue onto hazelnut shell: kinetics, mechanism and activation parameters, J. Hazard. Mater., 164 (2009) 172–181.

[51] S. Sobhanardakani, R. Zandipak, R. Sahraei, Removal of Janus Green dye from aqueous solutions using oxidized multi-walled carbon nanotubes, Tox. Environ. Chem., 95 (2013) 909–918.

[52] E. Daneshvar, A. Vazirzadeh, A. Niazi, M. Kousha, M. Naushad, A. Bhatnagar, Desorption of Methylene blue dye from brown macroalga: Effects of operating parameters, isotherm study and kinetic modeling, J. Clean. Prod., 152 (2017) 443–453.